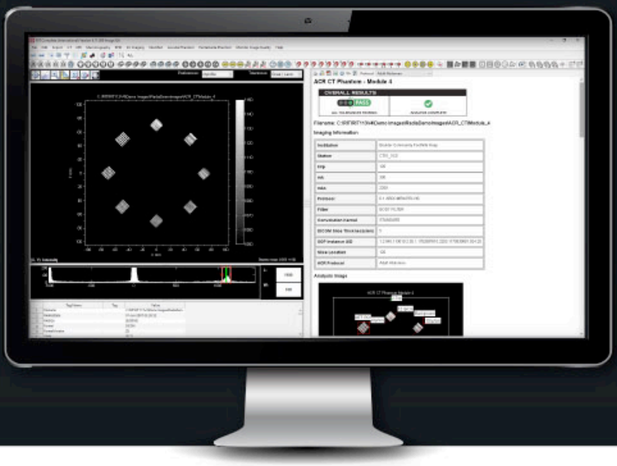

# Radia diagnostic

**Radia is an à la carte-based software for comprehensive imaging QC at your facility. Easily customize your Radia software by adding the diagnostic modules needed to perform automated analyses on your facility's phantoms.**

**Radia is tailored specifically for you.** Select and purchase any of the modules listed below to create a customized software package for your imaging QC needs. The software provides automated phantom analysis in seconds. Radia's simple, easy-to-use tools provide complete scoring of all phantom parameters with precision and accuracy. Full reports of all imaging tests are easily generated, and results can be automatically tracked with RIT*trend*™.

## DIAGNOSTIC MODULES & PHANTOMS

### ACR CT Module
- ACR CT Phantom

### ACR FFDM Module
- Gammex FFDM Phantom
- CIRS FFDM Phantom

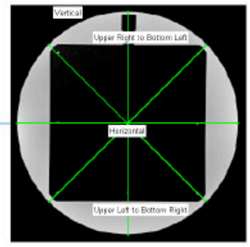


### ACR MR Module
- ACR Large MR Phantom

### ACR Small MRI Module
- ACR Small MRI Phantom (Extremity & Breast)

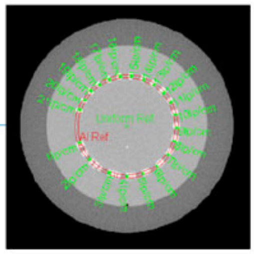

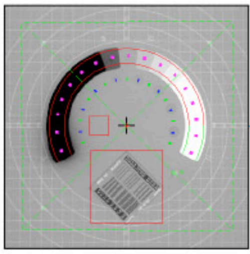

### Catphan/OBI Module
- CATPHAN® 500/600 Series Phantom
- Elekta 503 CATPHAN® (XVI) Phantom
- Varian 504 & 604 CATPHAN® Phantom
- Siemens MV CT (OBI) Phantom

### CT Uniformity Module
- Generic CT Water Phantoms

### Gamma Camera Uniformity Module
- None (Flood field)

### GE CT Module
- Optima 660 Phantom

### IEC 62464 MRI Module
- IEC 62464 MRI Phantom

### kV Imaging Module
- IBA Primus®-L Phantom
- Leeds TOR 18FG Phantom
- PTW NORMI® 4 Phantom (20 x 20 cm and 30 x 30 cm)
- Standard Imaging QCkV-1 Phantom

## AUTOMATION & CUSTOMIZATION FEATURES

### Hands-Free Automation
Use Cerberus to perform hands-free, fully automated phantom analysis. Cerberus automatically monitors folders, selects files based on your criteria, and analyzes them in the background of your machine.

### Batch Image Analysis
Use the RunQueueC Image Sequencer to perform one-click batch analysis on any number of images queued into the system. In seconds, each image slice of the phantom is analyzed automatically and the results exported to your preferred format.

### Tracking and Trending
RIT*trend*™ is the all-in-one statistical database solution for all of your department's measurements. Export full reports of all imaging tests with a single click and trend results over time.

### Tolerance Customization
RIT's Tolerance Manager sets tolerance values and pass/fail criteria for every measurement. Preference profiles can be precisely curated to each individual machine in use.

CLICK TO VISIT RADIMAGE.COM TO DEMO RIT'S ADVANCED RANGE OF MACHINE QA, MLC QA, PATIENT QA, AND IMAGING QA ROUTINES.


+1(719)590-1077, OPT. 4 SALES@RADIMAGE.COM

# Technical Note: Relative proton stopping power estimation from virtual monoenergetic images reconstructed from dual-layer computed tomography

Guillaume Landry and Fabian Dörringer
*Department of Medical Physics, Faculty of Physics, Ludwig-Maximilians-Universität München, Munich, Germany*

Salim Si-Mohamed and Philippe Douek
*Radiology Department, Centre Hospitalier Universitaire, Lyon, France*
*Univ Lyon, INSA-Lyon, Université Claude Bernard Lyon 1, UJM-Saint-Étienne, CNRS, Inserm, CREATIS UMR 5220, U1206, F-69373 Lyon, France*

Juan F. P. J. Abascal
*Univ Lyon, INSA-Lyon, Université Claude Bernard Lyon 1, UJM-Saint-Étienne, CNRS, Inserm, CREATIS UMR 5220, U1206, F-69373 Lyon, France*

Françoise Peyrin
*Univ Lyon, INSA-Lyon, Université Claude Bernard Lyon 1, UJM-Saint-Étienne, CNRS, Inserm, CREATIS UMR 5220, U1206, F-69373 Lyon, France*
*ESRF, The European Synchrotron, Grenoble, France*

Isabel P. Almeida and Frank Verhaegen
*Department of Radiation Oncology (MAASTRO), GROW School for Oncology and Developmental Biology, Maastricht University Medical Centre, Maastricht, The Netherlands*

Ilaria Rinaldi
*Department of Radiation Therapy and Oncology, Heidelberg University Hospital, Im Neuenheimer Feld 400, 69120 Heidelberg, Germany*
*CNRS/IN2P3 and Lyon 1 University, UMR 5822, Villeurbanne, France*
*MAASTRO Clinic, Dr. Tanslaan 12, 6229 ET Maastricht, The Netherlands*

Katia Parodi
*Department of Medical Physics, Faculty of Physics, Ludwig-Maximilians-Universität München, Munich, Germany*

Simon Rit[a)]
*Univ Lyon, INSA-Lyon, Université Claude Bernard Lyon 1, UJM-Saint-Étienne, CNRS, Inserm, CREATIS UMR 5220, U1206, F-69373 Lyon, France*

(Received 5 September 2018; revised 14 January 2019; accepted for publication 18 January 2019; published 19 February 2019)

**Purpose:** The objective of this technical note was to investigate the accuracy of proton stopping power relative to water (RSP) estimation using a novel dual-layer, dual-energy computed tomography (DL-DECT) scanner for potential use in proton therapy planning. DL-DECT allows dual-energy reconstruction from scans acquired at a single x-ray tube voltage $V$ by using two-layered detectors.
**Methods:** Sets of calibration and evaluation inserts were scanned at a DL-DECT scanner in a custom phantom with variable diameter $D$ (0 to 150 mm) at $V$ of 120 and 140 kV. Inserts were additionally scanned at a synchrotron computed tomography facility to obtain comparative linear attenuation coefficients for energies from 50 to 100 keV, and reference RSP was obtained using a carbon ion beam and variable water column. DL-DECT monoenergetic (mono-E) reconstructions were employed to obtain RSP by adapting the Yang–Saito–Landry (YSL) method. The method was compared to reference RSP via the root mean square error (RMSE) over insert mean values obtained from volumetric regions of interest. The accuracy of intermediate quantities such as the relative electron density (RED), effective atomic number (EAN), and the mono-E was additionally evaluated.
**Results:** The lung inserts showed higher errors for all quantities and we report RMSE excluding them. RMSE for $\mu$ from DL-DECT mono-E was below 1.9%. For the evaluation inserts at $D$ = 150 mm and $V$ = 140 kV, RED RMSE was 1.0%, while for EAN it was 2.9%. RSP RMSE was below 0.8% for all $D$ and $V$, which did not strongly affect the results.
**Conclusions:** In this investigation of RSP accuracy from DL-DECT, we have shown that RMSE below 1% can be achieved. It was possible to adapt the YSL method for DL-DECT and intermediate quantities RED and EAN had comparable accuracy to previous publications. © *2019 American Association of Physicists in Medicine* [https://doi.org/10.1002/mp.13404]

Key words: dual-energy CT, dual-layer CT, monoenergetic imaging, proton therapy, relative stopping power, synchrotron CT

## 1. INTRODUCTION

The recent interest of the proton therapy community in the measurement of relative stopping power (RSP) with spectral x-ray computed tomography (CT)[1,2] has seen the development of several methodologies following the seminal publications of Bazalova et al.[3], Yang et al.[4], and Hünemohr et al.[5] These methodologies pertain to scans acquired with more than one photon energy or spectrum and aim at reducing the RSP uncertainties attributed to single-energy CT (SECT).[6] Dual-energy CT (DECT) has been the standard modality so far, with the majority of publications pertaining to dual-source or dual-spiral technologies.[5,7–15] These image-based approaches have been recently validated using biological tissue samples[16–19] and have been found to consistently outperform SECT in terms of RSP accuracy. DECT scanners are currently making their way into proton therapy clinics[20] and may impact clinical proton range calculation.[8,21] Less attention has been paid to other DECT technologies such as rapid kV switching or dual-layer (DL) detectors, even though the latter allows for projection-based DECT algorithms, which are potentially superior to image-based procedures.[22] DL-DECT has recently been studied by Hua et al.[23] in terms of relative electron density (RED) and effective atomic number (EAN) accuracy and was found comparable to dual-source DECT. RSP has been investigated by Ohira et al.[24] but they did not evaluate the DL-DECT measurements against direct measurements of the RSP. In this technical note, we aimed at adapting a methodology for RSP estimation to DL-DECT data. We employed a different RED formalism than Hua et al.[23] (also used by Ohira et al.[24]) based on a calibration of the DL-DECT scanner via the virtual monoenergetic (mono-E) images typically reconstructed by DL-DECT.[25] We evaluated the final RSP by comparison to water column measurements in a carbon ion beam. Furthermore, the accuracy of the photon linear attenuation coefficients derived from the mono-E images underpinning our approach was evaluated by comparison to mono-E synchrotron CT scans.

## 2. MATERIALS AND METHODS

### 2.A. Phantoms

Two phantoms were built for mono-E synchrotron CT [Figs. 1(a), 1(b)] and DL- DECT [Fig. 1(c)] scans. The phantoms housed the tissue equivalent inserts listed in Table I in a low-density foam background for synchrotron CT and in a polyoxymethylene [POM, $(CH_2O)_n$, density 1.41 g·cm$^{-3}$] background for DL-DECT. The POM background diameter varied in 1 cm steps of $D = 0$ (bare inserts), 100, and 150 mm along the rotational axis of the phantom, allowing measurements with different diameters in one scan. The manufacturers' reference mass density ($\rho$), RED, EAN, and linear attenuation coefficient $\mu$ (at three photon energies) calculated from the manufacturers' stoichiometry are presented in Table I. The xraylib[26] was used to calculate $\mu$.

### 2.B. Synchrotron CT scans

Synchrotron CT images[27] were acquired on the ID17 beamline at the European Synchrotron Radiation Facility (ESRF). A double Si crystal monochromator was used to have a mono-E beam in 10 keV energy steps from 50 to 100 keV but we only report the results of 50, 80, and 100 keV for clarity. The beam was considered parallel given the large 145 m distance between the source and the object. The detector was an ESRF Frelon 2k camera with a 48-µm pixel size coupled with a gadolinium oxysulfide scintillator. The beam fully covered the 9.8-cm detector width but was only a few millimeters high (exact height varied depending on the energy, from 1.6 to 2.7 mm). The rotation axis was offset to obtain a 17-cm diameter field-of-view. Each scan consisted of 1200 projections equally distributed over 360°, each with $2048^2$ pixels. All axial slices covered by the beam were reconstructed with $840^2$ pixels and 0.2-mm isotropic pixel spacing using the filtered backprojection implementation of the reconstruction toolkit (RTK).[28]

### 2.C. Reference RSP

The RSP of each phantom insert was measured at the Heidelberg Ion-beam Therapy (HIT, Germany) using a PeakFinder water column (PTW, Freiburg, Germany). A carbon ion beam with 310.6 MeV/u energy was used to minimize the effect of multiple Coulomb scattering. Each depth dose profile of the water column was fitted with a fifth order polynomial and the 80% distal falloff was used to define the range. The methodology followed that of Hudobivnik et al.[8] and is detailed in appendix C of Vilches-Freixas.[29] The values are reported in the last column of Table I.

### 2.D. Dual-layer DECT scans

A clinical DL-DECT scanner (IQon Spectral CT, Philips Healthcare, Best, the Netherlands) was used to acquire scans of the phantoms with diameters ($D$) of 0, 100, and 150 mm at source voltages ($V$) 120 and 140 kV. The computed tomography index ($CTDI_{vol}$) was set to 20 mGy for all acquisitions, corresponding to an exposure of 200 mAs for 120 kV and 150 mAs at 140 kV. Exposure modulation was disabled. The pitch of the spiral scan was 1.17 and the collimation was set to 64 × 0.625 mm.

The DL-DECT scanner takes advantage of having the dual-energy measurements with exactly the same source and detector geometry (position and orientation) to apply the projection-based decomposition of Schlomka et al.[30] Following the model of Alvarez and Macovski,[31] line integrals of the Compton scatter (CS) and photoelectric effect (PE) maps are first decomposed from the acquired sinograms before tomographic reconstruction. This model assumes that the CS and PE maps are energy-independent quantities, and no beam-hardening correction is therefore required.

Mono-E images were reconstructed by the manufacturer's scanner software by applying the $\mu$ model using the reconstructed

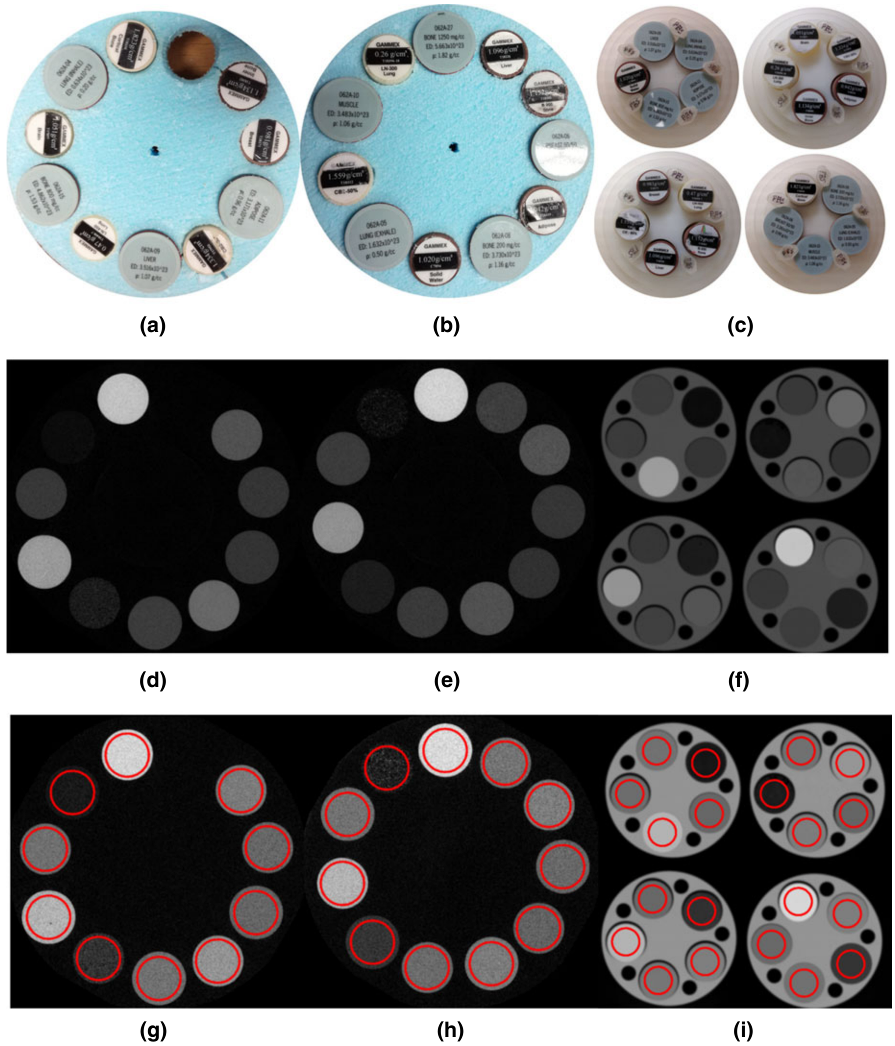


FIG. 1. Phantom configurations for (a, b) synchrotron computed tomography (CT) and (c) DL-DECT scans. (d, e, g, h) Synchrotron CT images reconstructed at (d, e) 50 keV and (g, h) 100 keV. (f, i) DL-DECT mono-E images acquired with $D = 100$ mm and $V = 140$ kV at (f) 50 keV and (i) 100 keV. Window/level set to (d)–(f) 1 cm$^{-1}$/0.5 cm$^{-1}$ and (g)–(i) 0.4 cm$^{-1}$/0.2 cm$^{-1}$. Volumetric regions of interest used for data analysis are shown in red. (c) The POM background steps of $D = 0$ (bare inserts), 100, and 150 mm are visible. [Color figure can be viewed at wileyonlinelibrary.com]

CS and PE maps, at 10 keV increments from 40 to 200 keV, with a slice thickness of 1.5 mm, in-slice pixel dimensions of 0.3 mm × 0.3 mm and 512 × 512 pixels. We employed the Philips' iDose reconstruction software with level 5 and the standard B filter.

### 2.E. Conversion of DL-DECT data to RSP

Our RSP estimation procedure followed the previously published combination of methods of Yang et al.[4], Saito,[32] and Landry et al.[33] (YSL, see e.g., Hudobivnik et al.[8]) which have been previously applied to dual-source or dual-spiral datasets.[34]

The mono-E images reconstructed by the DL-DECT scanner software are linear combinations of two bases approximating CS and PE contributions to the linear attenuation coefficient, as explained in Hua et al.[23] Hua et al.[23] used a linear combination of CS and PE to obtain RED; however, CS and PE were not directly accessible from the DL-DECT software. To circumvent this, we relied on a linear combination of an optimal pair of mono-E images using the formalism of Saito[32] for RED estimation. The fit parameters of Saito[32] were obtained from a procedure based on the calibration of the scanner using the insert data of the Gammex inserts. Since the mono-E images are themselves linear combinations of the CS and PE bases, their linear combination should allow similar results as Hua et al.[23] The chosen energy pair, 50 and 200 keV from the 140 kV and 150 mm diameter phantom, maximized the coefficient of determination of the Saito[32] fit and was the same as in Mei et al.[25]

We used the same pair of mono-E images to calculate the ratio of relative linear attenuation coefficients $\frac{(\mu/\mu_{\text{water}})_{50\text{ keV}}}{(\mu/\mu_{\text{water}})_{200\text{ keV}}}$ as in Joshi et al.[35] and Hua et al.[23] and fitted to the EAN of our Gammex inserts with a fourth-order polynomial. This is equivalent to the procedure described in Landry et al.[33] which is typically employed in the YSL method.

TABLE I. List of phantom insert materials used in this study, their mass density ($\rho$), and relative electron density (RED) provided by the manufacturers, effective atomic number (EAN) and linear attenuation coefficient $\mu_{ref}$ computed from the manufacturers' stoichiometry, and relative stopping power (RSP) measured using a carbon ion beam and a water column.

| | | | | $\mu$ (cm$^{-1}$) | | | |
|---|---|---|---|---|---|---|---|
| Name | $\rho$ (g.cm$^{-3}$) | RED | EAN | 50 keV | 80 keV | 100 keV | RSP |
| Gammex | | | | | | | |
| LN-300 | 0.300 | 0.292 | 7.8 | 0.067 | 0.054 | 0.050 | 0.248 |
| LN-450 | 0.450 | 0.438 | 7.7 | 0.100 | 0.081 | 0.075 | 0.455 |
| AP6 | 0.940 | 0.922 | 6.4 | 0.193 | 0.165 | 0.155 | 0.941 |
| BR-12 | 0.980 | 0.957 | 7.1 | 0.209 | 0.174 | 0.162 | 0.971 |
| Solid water | 1.020 | 0.990 | 7.9 | 0.229 | 0.183 | 0.169 | 1.000 |
| BRN-SR2 | 1.050 | 1.046 | 6.3 | 0.218 | 0.187 | 0.176 | 1.062 |
| LV1 | 1.100 | 1.069 | 7.9 | 0.247 | 0.197 | 0.183 | 1.076 |
| IB3 | 1.140 | 1.093 | 10.6 | 0.328 | 0.220 | 0.197 | 1.083 |
| B200 | 1.150 | 1.102 | 10.6 | 0.331 | 0.222 | 0.198 | 1.094 |
| CB2-30 | 1.340 | 1.285 | 11.1 | 0.408 | 0.265 | 0.234 | 1.258 |
| CB2-50 | 1.560 | 1.470 | 12.7 | 0.577 | 0.330 | 0.282 | 1.427 |
| CIRS | | | | | | | |
| Lung inhale | 0.195 | 0.191 | 7.1 | 0.041 | 0.035 | 0.032 | 0.207 |
| Lung exhale | 0.510 | 0.499 | 7.7 | 0.114 | 0.092 | 0.085 | 0.483 |
| Adipose | 0.960 | 0.949 | 6.6 | 0.201 | 0.171 | 0.160 | 0.967 |
| Breast | 0.991 | 0.976 | 7.1 | 0.213 | 0.177 | 0.165 | 0.992 |
| Muscle | 1.062 | 1.042 | 7.8 | 0.238 | 0.191 | 0.178 | 1.045 |
| Liver | 1.072 | 1.051 | 7.8 | 0.240 | 0.193 | 0.179 | 1.056 |
| Trabecular bone | 1.161 | 1.116 | 10.6 | 0.331 | 0.224 | 0.200 | 1.094 |
| Bone 800 | 1.530 | 1.450 | 14.1 | 0.635 | 0.344 | 0.288 | 1.401 |

Finally, the EAN was converted to ln($I$), where $I$ is the mean excitation potential, using the approach of Yang et al.[4] with the same fit employed in Hudobivnik et al.[8] Both ln($I$) and RED were used with the Bethe equation with $I_{water}$ = 78 eV[36] and $\beta = 0.428$ (100 MeV proton energy) to obtain RSP [see eq. (4) in Hudobivnik et al.[8]]

### 2.F. Data evaluation

Using the calibration obtained for the $V = 140$ kV and $D = 150$ mm diameter calibration inserts, we computed RED, EAN, and RSP for the remaining configurations of the phantoms and for the evaluation inserts, under the assumption that the reconstructed mono-E should ideally be equivalent for all protocols.

Volumetric regions of interest (ROI) covering the central part of each insert were used to extract the mean and the standard deviation of the mono-E, RED, EAN, and RSP images [Figs. 1(g), 1(h), 1(i)]. The accuracy of each quantity was evaluated by calculating the residual relative error:

$$\text{residuals} = \frac{\text{value}_{\text{meas}} - \text{value}_{\text{ref}}}{\text{value}_{\text{ref}}} \cdot 100\% \quad (1)$$

where $\text{value}_{\text{meas}}$ are the mean values in each insert ROI and $\text{value}_{\text{ref}}$ are the reference values obtained from stoichiometry (RED, EAN, and $\mu$) or water column measurements (RSP) (see Hudobivnik et al.[8] for the definitions used for reference EAN and RED calculations). We additionally calculated the root mean square error (RMSE) for each phantom dataset (combination of phantom, $D$ and $V$) with:

$$\text{RMSE} = \sqrt{\frac{\sum_i^{N_{\text{inserts}}} \text{residuals}_i^2}{N_{\text{inserts}}}} \quad (2)$$

where $N_{\text{inserts}}$ are the number of inserts $i$ of each phantom.

## 3. RESULTS

### 3.A. Mono-E accuracy

Figure 2 presents the residuals of $\mu$ obtained from DL-DECT and synchrotron CT mono-E reconstructions with the manufacturers' stoichiometry as a reference. The largest errors were for the lung inserts, with an absolute maximum of 16% and 20% at 80 keV for DL-DECT and synchrotron CT, respectively. Excluding lung inserts, all absolute errors were below 6%. The RMSE of DL-DECT was 4.5%/4.5%/4.6% at 50/80/100 keV and the RMSE of synchrotron CT 5.4%/5.6%/3.6% with all inserts, and 1.9%/1.0%/1.0% and 2.8%/3.0%/2.3% without the lung inserts, respectively. With all inserts, the bias (signed average) was always negative, with −0.7%/–0.4%/–0.5% at 50/80/100 keV for DL-DECT and −3.1%/–3.6%/–1.7% for synchrotron CT. The bias was not significant for DL-DECT (paired Student $t$-test, $P > 0.08$) and was significant for synchrotron CT ($P < 0.001$).

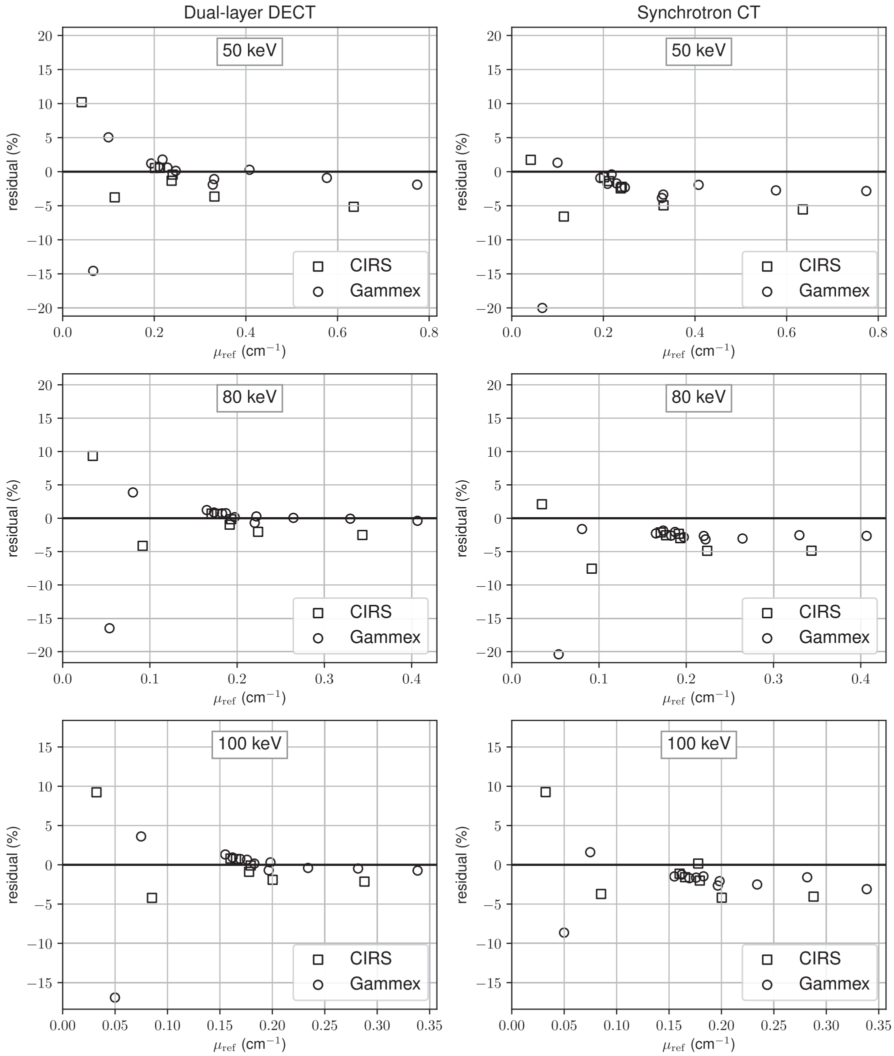


FIG. 2. Residual of the monoenergetic linear attenuation coefficient $\mu$ measured with the dual-layer DECT and synchrotron computed tomography (CT) as a function of $\mu_{\rm ref}$ calculated from the manufacturers' stoichiometry. Three energies are shown: 50 keV (top), 80 keV (middle), and 100 keV (bottom). The standard error of the mean was below 0.2% for DL-DECT and below 0.5% for synchrotron CT.

## 3.B. EAN, RED, and RSP accuracy

Figure 3 presents the residuals of RED, EAN, and RSP for the evaluation inserts and Table II reports the RMSE for both sets of inserts. The typically poor results for the porous lung substitutes previously reported in DECT studies were also observed here. For this reason, RMSE is reported in Table II with and without these inserts. The following results

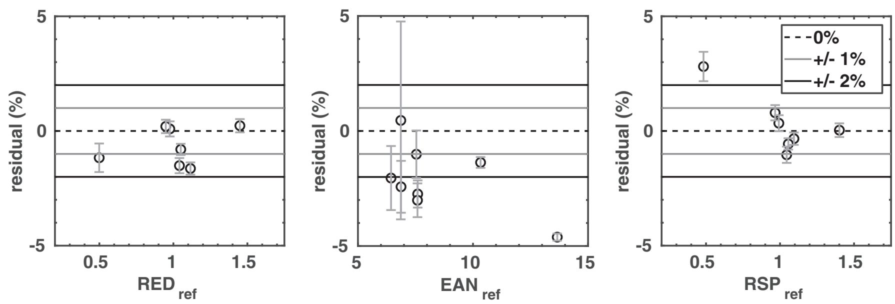


FIG. 3. Relative electron density (RED), effective atomic number (EAN), and relative stopping power (RSP) residuals as a function of the reference values of the evaluation inserts. Results for source voltage ($V$) of 140 kV and phantom diameter ($D$) of 150 mm are presented. The error bars correspond to the standard deviation of the distribution of values in each insert regions of interest. The lowest density lung inserts, not visible in the RED and RSP plots, had residual RED/EAN/RSP of 23%/0.5%/15%.

TABLE II. RMSE for RED, EAN, and RSP of the calibration and evaluation inserts for the $D$ = 150 mm and $V$ = 140 kV configuration. Results with and without lung inserts are reported.

| Phantom | RED | EAN | RSP |
|---|---|---|---|
| Gammex | 3.3% | 2.0% | 2.6% |
| CIRS | 8.1% | 2.5% | 5.4% |
| Excluding lung inserts in RMSE calculation | | | |
| Gammex | 0.5% | 1.7% | 0.6% |
| CIRS | 1.0% | 2.9% | 0.6% |
| Excluding lung inserts in calibration and RMSE calculation | | | |
| Gammex | 0.4% | 1.2% | 0.7% |
| CIRS | 0.9% | 2.0% | 0.6% |

TABLE III. RMSE of RSP for different $V$ and $D$ excluding lung inserts in the calculation of RMSE.

| | $V$ = 120 kV | | $V$ = 140 kV | |
|---|---|---|---|---|
| $D$ (mm) | Gammex | CIRS | Gammex | CIRS |
| 0 | 0.8% | 0.8% | 0.7% | 0.6% |
| 100 | 1.0% | 0.5% | 0.8% | 0.6% |
| 150 | 0.7% | 0.7% | 0.6% | 0.6% |

refer to the $D$ = 150 mm and $V$ = 140 kV configuration shown in Fig. 3.

The RED residuals were contained within 2%. The RED error was 23% for the lowest density lung insert (CIRS Lung inhale); however, the higher density lung insert (CIRS Lung exhale) exhibited similar residuals as the other inserts. The RMSE was ≤1.0% when excluding lung inserts (see Table II), compared to 0.5% for the calibration inserts.

For EAN, several evaluation inserts had errors larger than −2%, ranging up to −5%, and the lung inserts did not exhibit increased residuals in this case. The RMSE for EAN was increased from 2.5% to 2.9% when excluding the lung inserts from the evaluation set, while for the calibration set it decreased from 2% to 1.7%.

For RSP, the main quantity of interest in this work, all non-lung inserts had residuals within ±2% for the evaluation set. The RMSE without lung inserts was 0.6% for both evaluation and calibration inserts. The lowest density lung insert had a RSP error of 15%. Changing the diameter $D$ and voltage $V$ had negligible impact on RSP RMSE (Table III). Table II additionally shows that excluding the lung inserts entirely from the calibration and evaluation procedures had little impact on RSP RMSE.

## 4. DISCUSSION

In this report on the potential use of DL-DECT for proton therapy, the RSP accuracy achieved was better than 2% for all inserts and for all scan configurations, barring the lung substitutes (CIRS Lung inhale and Lung exhale, Gammex LN-300 and LN-450). Unless specified otherwise, the following discussion points will assume that the lung substitute inserts are omitted. The poor accuracy achieved with lung mimicking inserts, mainly related to their heterogeneity, can be found in several reports.[8,23,34] These errors may be caused by the nonlinear impact of partial volume effects caused by the fine structure of the porous material employed to mimic lungs.[37] Since proton therapy of the lung also suffers from more important uncertainties related to breathing motion, it is unclear whether the use of DECT is critical for these cases. Table II shows that excluding the lung inserts completely from the calibration process has little impact on RSP accuracy.

The $V$ = 140 kV and $D$ = 150 mm DL-DECT calibration and evaluation inserts RMSE presented in this work, both 0.6%, are comparable to state-of-the-art DECT-based RSP estimation.[8] There were no RSP RMSE higher than 1.0% for the range of background material diameters we investigated, which cover dimensions relevant for proton therapy of brain and head and neck cancer patients. Ohira et al.[24] reported similar results with DL-DECT using stoichiometry as a reference and the same inserts for calibration and evaluation of EAN.

We made use of the ICRU-recommended value of 78 eV[36] for $I_{water}$ when calculating RSP from DL-DECT scans. When using the Bragg additivity rule with the ICRU-recommended elemental $I$ values for compounds, one obtains $I_{water}$ = 75 eV, which yields validation set RSP RMSE without lung inserts of 0.9%, compared to 0.6% with 78 eV. The recent work of Bär et al.[38] proposes updated elemental $I$ values which yield $I_{water}$ = 78 eV with the Bragg rule, but were not employed in this work.

A synchrotron CT was used to compare the accuracy of DL-DECT mono-E images in the 50–100 keV range. Our results indicate that DL-DECT can measure mono-E values which are consistent with those measured on a mono-E beam, and potentially with higher accuracy if we assume that the stoichiometry from the phantom manufacturers is accurate as a reference. One possible source of underestimation of the linear attenuation coefficient $\mu_{ref}$ by synchrotron CT is the measurement of scattered radiation since the distance between the sample and the detector was kept low (<1 m) to limit phase contrast artifacts in the measured projection images. An alternative approach to avoid scatter would be the use of a pencil beam to measure $\mu$ in the projection domain, similarly to the measurement of RSP on a carbon ion beam. This measurement is, however, more sensitive to insert dimension uncertainties than for RSP given the exponential nature of attenuation.

Even though we make use of pairs of mono-E images in this work, our approach is not strictly image-based since the linear combination of the mono-E pair used to calculate RED is an indirect manipulation of the CS and PE bases. Furthermore, since most DECT scanners provide mono-E reconstruction as a standard feature, our methods could easily be generalized to any scanner model.

In terms of noise, we do not expect that DL-DECT would perform better than state-of-the-art dual-source systems, since

Jacobsen et al.[39] showed higher noise levels for the scanner model considered in this study compared to dual-source scanners for mono-E images. The increased noise would naturally yield increased RSP noise. This was however outside the scope of this study.

Finally, when considering the results presented in this study, it is important to note that for RED, EAN, and $\mu$, reference values were calculated from manufacturer-reported stoichiometry, while for RSP we relied on reference measurements. This means that insert-specific errors seen in the RED, EAN, or $\mu$ may not correlate to those observed for RSP. Furthermore, we have validated our calibration with a set of evaluation inserts based on epoxy-based tissue mimicking inserts similar to those used for calibration. There is thus room to extend our validation to real tissues, ideally using animal samples.

## 5. CONCLUSION

DL-DECT provided RSP accuracy comparable to state-of-the-art dual-source DECT scanners for phantom sizes relevant for brain and head-and-neck cancer proton therapy. The RMSE when ignoring lung inserts was 0.6% for our evaluation and calibration inserts. It was possible to adapt standard DECT RSP calculation methods to the images produced by the DL-DECT by leveraging mono-E images reconstructed at 50 keV and 200 keV. Intermediate quantities RED and EAN were estimated with similar accuracy as previously published for DL-DECT, and $\mu$ accuracy was comparable or better than that achieved with mono-E synchrotron CT.

## ACKNOWLEDGMENTS

The authors thank the Heidelberg Ion-Beam Therapy Center (HIT) for allocated beam time, and we are grateful to Stefan Brons for local experimental support and Gloria Vilches-Freixas for assistance in measuring the reference water equivalent thickness values of the phantom inserts. The authors also thank the European Synchrotron Radiation Facility for allocated beam time within the experiment MD1045 at the beamline ID17, and we are grateful to Alberto Bravin, Claude Goubet, Tom Hohweiller, Cyril Mory, Cécile Olivier, Odran Pivot, and Herwig Requardt for assistance in acquiring synchrotron CT images. This work was supported by the German Research Foundation's (DFG) Cluster of Excellence Munich-Centre for Advanced Photonics (MAP) and by the Bavaria-France Cooperation Centre (BFHZ). JFPJ Abascal has received funding from the European Union's Horizon 2020 Research and Innovation programme under the Marie Sklodowska-Curie grant agreement No. 701915. This work was performed within the framework of the LABEX PRIMES (ANR-11-LABX-0063) of Université de Lyon, within the program "Investissements d'Avenir" (ANR-11-IDEX-0007) operated by the French National Research Agency (ANR).

[a]Author to whom correspondence should be addressed. Electronic mail: simon.rit@creatis.insa-lyon.fr.

## REFERENCES

1. van Elmpt W, Landry G, Das M, Verhaegen F. Dual energy CT in radiotherapy: current applications and future outlook. *Radiother Oncol*. 2016;119:137–144.
2. Taasti VT, Bäumer C, Dahlgren CV, et al. Inter-centre variability of CT-based stopping-power prediction in particle therapy: survey-based evaluation. *Phys Imaging Radiat Oncol*. 2018;6:25–30.
3. Bazalova M, Carrier J-F, Beaulieu L, Verhaegen F. Dual-energy CT-based material extraction for tissue segmentation in Monte Carlo dose calculations. *Phys Med Biol*. 2008;53:2439.
4. Yang M, Virshup G, Clayton J, Zhu XR, Mohan R, Dong L. Theoretical variance analysis of single-and dual-energy computed tomography methods for calculating proton stopping power ratios of biological tissues. *Phys Med Biol*. 2010;55:1343.
5. Hünemohr N, Krauss B, Tremmel C, Ackermann B, Jäkel O, Greilich S. Experimental verification of ion stopping power prediction from dual energy CT data in tissue surrogates. *Phys Med Biol*. 2013;59:83.
6. Yang M, Zhu XR, Park PC, et al. Comprehensive analysis of proton range uncertainties related to patient stopping-power-ratio estimation using the stoichiometric calibration. *Phys Med Biol*. 2012;57:4095.
7. Bourque AE, Carrier J-F, Bouchard H. A stoichiometric calibration method for dual energy computed tomography. *Phys Med Biol*. 2014;59:2059.
8. Hudobivnik N, Schwarz F, Johnson T, et al. Comparison of proton therapy treatment planning for head tumors with a pencil beam algorithm on dual and single energy CT images. *Med Phys*. 2016;43:495–504.
9. Möhler C, Wohlfahrt P, Richter C, Greilich S. Range prediction for tissue mixtures based on dual-energy CT. *Phys Med Biol*. 2016;61:N268.
10. Han D, Siebers JV, Williamson JF. A linear, separable two-parameter model for dual energy CT imaging of proton stopping power computation. *Med Phys*. 2016;43:600–612.
11. Taasti VT, Petersen JBB, Muren LP, Thygesen J, Hansen DC. A robust empirical parametrization of proton stopping power using dual energy CT. *Med Phys*. 2016;43:5547–5560.
12. Lalonde A, Bouchard H. A general method to derive tissue parameters for Monte Carlo dose calculation with multi-energy CT. *Phys Med Biol*. 2016;61:8044.
13. Lalonde A, Bär E, Bouchard H. A Bayesian approach to solve proton stopping powers from noisy multi-energy CT data. *Med Phys*. 2017;44:5293–5302.
14. Saito M, Sagara S. Simplified derivation of stopping power ratio in the human body from dual-energy CT data. *Med Phys*. 2017;44:4179–4187.
15. Almeida IP, Schyns LEJR, Vaniqui A, et al. Monte Carlo proton dose calculations using a radiotherapy specific dual-energy CT scanner for tissue segmentation and range assessment. *Phys Med Biol*. 2018; 63:115008.
16. Taasti VT, Michalak GJ, Hansen DC, et al. Validation of proton stopping power ratio estimation based on dual energy CT using fresh tissue samples. *Phys Med Biol*. 2017;63:015012.
17. Bär E, Lalonde A, Zhang R, et al. Experimental validation of two dualenergy CT methods for proton therapy using heterogeneous tissue samples. *Med Phys*. 2018;45:48–59.
18. Xie Y, Ainsley C, Yin L, et al. Ex vivo validation of a stoichiometric dual energy CT proton stopping power ratio calibration. *Phys Med Biol*. 2018;63:055016.
19. Möhler C, Russ T, Wohlfahrt P, et al. Experimental verification of stopping-power prediction from single-and dual-energy computed tomography in biological tissues. *Phys Med Biol*. 2018;63:025001.
20. Wohlfahrt P, Möhler C, Hietschold V, et al. Clinical implementation of dual-energy CT for proton treatment planning on pseudo-monoenergetic CT scans. *Int J Radiat Oncol Biol Phys*. 2017;97:427–434.
21. Wohlfahrt P, Möhler C, Stützer K, Greilich S, Richter C. Dual-energy CT based proton range prediction in head and pelvic tumor patients. *Radiother Oncol*. 2017;125:526–533.
22. Vilches-Freixas G, Taasti VT, Muren LP, et al. Comparison of projection-and image-based methods for proton stopping power estimation using dual energy CT. *Phys Imaging Radiat Oncol*. 2017;3:28–36.
23. Hua C, Shapira N, Merchant TE, Klahr P, Yagil Y. Accuracy of electron density, effective atomic number, and iodine concentration determination with a dual-layer dual-energy computed tomography system. *Med Phys*. 2018;45:2486–2497.

24. Ohira S, Washio H, Yagi M, et al. Estimation of electron density, effective atomic number and stopping power ratio using dual-layer computed tomography for radiotherapy treatment planning. *Phys Med*. 2018;56:34–40.
25. Mei K, Ehn S, Oechsner M, et al. Dual-layer spectral computed tomography: measuring relative electron density. *Eur Radiol Exper*. 2018;2:20.
26. Schoonjans T, Brunetti A, Golosio B, et al. The xraylib library for X-ray–matter interactions. recent developments. *Spectrochim Acta, Part B*. 2011;66:776–784.
27. Salomé M, Peyrin F, Cloetens P, et al. A synchrotron radiation microtomography system for the analysis of trabecular bone samples. *Med Phys*. 1999;26:2194–2204.
28. Rit S, Oliva MV, Brousmiche S, Labarbe R, Sarrut D, Sharp GC. The reconstruction toolkit (RTK), an open-source cone-beam CT reconstruction toolkit based on the insight toolkit (ITK). *J Phys*. 2014;489:012079.
29. Vilches-Freixas G. *Dual-energy cone-beam CT for proton therapy*. PhD thesis, Institut National des Sciences Appliquées (INSA) de Lyon; 2017. URL http://theses.insa-lyon.fr/publication/2017LYSEI099/these.pdf
30. Schlomka JP, Roessl E, Dorscheid R, et al. Experimental feasibility of multi-energy photon-counting K-edge imaging in pre-clinical computed tomography. *Phys Med Biol*. 2008;53:4031–4047.
31. Alvarez RE, Macovski A. Energy-selective reconstructions in X-ray computerized tomography. *Phys Med Biol*. 1976;21:733–744.
32. Saito M. Potential of dual-energy subtraction for converting CT numbers to electron density based on a single linear relationship. *Med Phys*. 2012;39:2021–2030.
33. Landry G, Seco J, Gaudreault M, Verhaegen F. Deriving effective atomic numbers from DECT based on a parameterization of the ratio of high and low linear attenuation coefficients. *Phys Med Biol*. 2013;58:6851.
34. Almeida IP, Schyns LEJR, Öllers MC, et al. Dual-energy CT quantitative imaging: a comparison study between twin-beam and dual-source CT scanners. *Med Phys*. 2017;44:171–179.
35. Joshi M, Langan DA, Sahani DS, et al. Effective atomic number accuracy for kidney stone characterization using spectral CT. In: *Proc. SPIE 7622, Medical Imaging 2010: Physics of Medical Imaging, 76223K*; 2010.
36. Sigmund P, Schinner A, Paul H. Errata and addenda for ICRU report 73, stopping of ions heavier than helium. *J ICRU*. 2009;5:1–10.
37. Persson M, Holmin S, Karlsson S, Bornefalk H, Danielsson M. Subpixel x-ray imaging with an energy-resolving detector. *J Med Imaging*. 2018;5:013507.
38. Bär E, Andreo P, Lalonde A, Royle G, Bouchard H. Optimized I-values for use with the Bragg additivity rule and their impact on proton stopping power and range uncertainty. *Phys Med Biol*. 2018;63:165007.
39. Jacobsen MC, Schellingerhout S, Wood CA, et al. Intermanufacturer comparison of dual-energy CT iodine quantification and monochromatic attenuation: a phantom study. *Radiology*. 2018;287:224–234.